Confidential: not for distribution. Submitted to the American Astronomical Society for peer review 2009 July 24

Constraining Intra-cluster Gas Models with AMiBA13

Sandor M. Molnar[1], Keiichi Umetsu[1,2], Mark Birkinshaw[3], Greg Bryan[4], Zoltán Haiman[4],
Nathan Hearn[5], Cien Shang[4], Paul T.P. Ho[1,6], Chih-Wei Locutus Huang[7,2],
Patrick M. Koch[1], Yu-Wei Victor Liao[7,2], Kai-Yang Lin[1], Guo-Chin Liu[1,8],
Hiroaki Nishioka[1], Fu-Cheng Wang[7], Jiun-Huei Proty Wu[7,2]

`sandor@asiaa.sinica.edu.tw`

ABSTRACT

Clusters of galaxies have been used extensively to determine cosmological parameters. A major difficulty in using Sunyaev–Zel′dovich (SZ) and X-ray observations of clusters for cosmology is in the determination of the physical properties of the intra-cluster gas (ICG) out to the virial radius. Using X–ray observations it is difficult to measure the temperature distribution and therefore determine the density distribution in individual clusters of galaxies out to the virial radius. Observations with the new generation of SZ instruments are a promising alternative approach. We use clusters of galaxies drawn from high-resolution adaptive mesh refinement (AMR) cosmological simulations to study how well we should be able to constrain the large-scale distribution of the ICG in individual massive relaxed clusters using AMiBA, after its upgrade to 13 elements with 1.2-m diameter dishes (AMiBA13). We show that non-isothermal β models provide a good description of the ICG in our simulated relaxed clusters. We use simulated X-ray observations to constrain the distribution of the gas density, and simulated

---

[1] Institute of Astronomy and Astrophysics, Academia Sinica, P.O. Box 23-141, Taipei 106, Taiwan, ROC.; sandor@asiaa.sinica.edu.tw

[2] Leung center for Cosmology and Particle Astrophysics, National Taiwan University, Taipei 10617, Taiwan, ROC.

[3] Department of Physics, University of Bristol, Tyndall Ave, Bristol BS8 1TL, UK

[4] Department of Astronomy, Columbia University, 550 West 120th Street, New York, NY 10027

[5] ASC/Alliances Center for Astrophysical Thermonuclear Flashes, University of Chicago, Chicago IL 60637

[6] Harvard-Smithsonian Center for Astrophysics, 60 Garden Street, Cambridge, MA 02138

[7] Department of Physics, Institute of Astrophysics, & Center for Theoretical Sciences, National Taiwan University, Taipei 10617, Taiwan, ROC.

[8] Department of Physics, Tamkang University, 251-37, Tamsui, Taipei County, Taiwan, ROC.

SZ visibilities (AMiBA13 observations) to constrain the large-scale temperature distribution of the ICG. We find that AMiBA13 visibilities should constrain the scale radius of the temperature distribution to about 50% statistical accuracy (68% confidence level). We conclude that AMiBA, after its upgrade to AMiBA13, should be a powerful instrument to constrain the large-scale distribution of the ICG.

Subject headings: galaxies: clusters: general

1. Introduction

According to our standard structure formation scenarios based on the dark matter (DM) models, clusters of galaxies, the most massive virialized objects in the Universe, form from the largest positive density fluctuations, thus their formation and evolution are sensitive to the underlying cosmological model. Taking advantage of this feature, clusters have been used extensively to determine cosmological parameters (e.g., Henry 2000; Allen et al. 2004; Ettori 2004; Vikhlinin et al. 2008; for recent reviews see Voit 2005 & Borgani 2006). Prospects of determining cosmological parameters using much larger samples of clusters of galaxies from next generation surveys were discussed in detail by e.g., Haiman, Mohr & Holder (2001); Holder, Haiman & Mohr (2001); Molnar, Birkinshaw & Mushotzky (2002) and Molnar et al. (2004). While theory predicts the mass function of clusters of galaxies and the distribution of mass, gas density and temperature within individual clusters, observations directly measure the X-ray luminosity and intra-cluster gas temperature functions, luminosity functions based on the Sunyaev-Zel′dovich (SZ) effect, and the projected distribution of X-ray emissivity and electron pressure. To connect theory and observations it is crucial to understand the physics of clusters out to their virial radii and beyond. The observed large-scale distribution of the intra-cluster gas (ICG) and its evolution can be directly compared to predictions of our cosmological structure formation models and so constrain them.

In this paper we carry out a feasibility study to estimate how well we should be able to constrain the large-scale distribution of the ICG using data to be taken with the Yuan-Tseh Lee Array for Microwave Background Anisotropy (AMiBA; Ho et al. 2009; Wu et al. 2009) interferometer operating at 94 GHz with the planned upgrade to 13 antennas (AMiBA13; Koch et al., in preparation). In this paper we first summarize the presently available observational constraints on the large-scale distribution of the ICG (§2). In section §3 we derive a family of models for the ICG from our high-resolution cosmological simulations. We then present our methods of generating SZ and X-ray images of simulated clusters of galaxies in §4. Our method to simulate visibilities for mock AMiBA13 observations is described in §5. Model fitting and the results are presented in section §6. Finally, in section §7, we discuss our results for the constraints on the shape parameters of our ICG models from mock AMiBA13 observations.

Our companion papers describe the details of the design, performance, and the science results from the first observational season of AMiBA with the first configuration (AMiBA7). Ho et al. (2009) describe the design concepts and specifications of the AMiBA telescope. Technical aspects of the instruments are described by Chen et al. (2009) and Koch et al. (2009a). Details of the first SZ observations and data analysis are presented by Wu et al. (2009). Nishioka et al. (2009) assess the integrity of AMiBA7 data performing several statistical tests. Lin et al. (2009) discuss the system performance and verification. Contamination from foreground sources and the primary cosmic microwave background (CMB) fluctuations is estimated by Liu et al. (2009). Koch et al. (2009b) present a measurement of the Hubble constant using AMiBA7 and archival X-ray data. Umetsu et al. (2009) determine gas mass fractions using gravitational lensing and AMiBA7 observations of galaxy clusters. Huang et al. (2009) discuss cluster scaling relations between AMiBA7 and X-ray data.

2. Constraints on the large-scale Distribution of the Intra-Cluster Gas

Thermal bremsstrahlung is generated by the scattering of two particles (an electron and an ion) in the ICG, thus the X-ray emission is proportional to the square of the electron density, since the ion density is proportional to the electron density (e.g., Sarazin 1988). The SZ effect, the inverse-Compton scattering of cold photons of the CMB by electrons in the hot ICG, is proportional to the electron density (Sunyaev & Zel'dovich 1980; for recent reviews see Rephaeli 1995; Birkinshaw 1999; and Carlstrom, Holder & Reese 2002). As a consequence, X-ray observations are more sensitive to the inner parts of clusters, while SZ observations are also sensitive to the outer regions. The X-ray flux is dominated by signal from regions with $0.1 \lesssim r/R_{\rm vir} \lesssim 0.4$, where the virial radius, $R_{\rm vir}$, is defined here according to the usage in Bryan & Norman (1998), and the total SZ decrement is dominated by signal from regions near $R_{\rm vir}$ (see Figure 10 of Fang & Haiman 2008).

We measure the SZ signal, which is proportional to the line-of-sight (LOS) integral of the electron pressure, and the X-ray surface brightness, which is proportional to the LOS integral of the X-ray emissivity. The projections cause the observables to depend on the LOS size of the cluster. This size can be estimated based on the angular size from the X-ray or SZ image and the angular diameter distance to the cluster, D_A. The X-ray and SZ brightnesses of the cluster then provide two equations from which we can estimate two unknowns, D_A

and some characteristic electron density in the cluster. Observing a sample of clusters, we can derive D_A as a function of the redshift, z, and thus constrain cosmological parameters. This is usually called the SZ–X–ray (SZX) method (e.g., Birkinshaw 1999; see Koch et al. 2009b for an application of this method using AMiBA7 observations).

In practical implementations of the SZX method, we determine the spatial model for the cluster from the higher signal-to-noise (SN) X-ray observations, which typically go out to about half of the virial radius. The caveat of this method is that there is no guarantee that the ICG distribution at large radii follows an extrapolation of the distribution determined from X-ray data. Also, due to projection effects, measurement errors, etc., the distribution of the ICG determined from X-ray measurements might be biased. Models used to describe the X-ray observations of clusters are typically β models for the density distribution, $\rho_g \propto (1 + r^2/{r_{\rm core}}^2)^{-3\beta/2}$, where the core radius, $r_{\rm core}$, and β are fitting parameters (Cavaliere & Fusco-Femiano 1976); with either constant temperature (isothermal β models), or a gradually declining temperature as a function of the distance from the cluster center. The resulting β parameters are in the range of 0.5 - 0.8 typically. Many relaxed clusters have $\beta \approx 2/3$, which provides a shallow density profile, $\rho \propto r^{-2}$, at large radii (e.g., Sarazin 1988; for recent results see Maughan et al. 2008 and references therein).

However, numerical simulations, SZ and X-ray observations suggest a much steeper fall off of the density at large radii. Roncarelli et al. (2006) used a sample of 9 clusters of galaxies in the mass range of 1.5×10^{14} $\mathrm{M}_\odot$ – 3.4×10^{15} $\mathrm{M}_\odot$ from smoothed particle hydrodynamic simulations (SPH) to derive gas density and temperature profiles in the outskirts of clusters. They used simulations with and without cooling, supernova feedback and thermal heat conduction. Roncarelli et al. found that these profiles steepen as a function of radius. They also found that cooling and supernova feedback do not affect the density and temperature profiles at large radii significantly. Their results support the theoretical expectation that the distribution of gas at large radii in clusters of galaxies is determined mainly by gravity. Hallman et al. (2007) fitted isothermal β models to mock X-ray and SZ observations of simulated clusters drawn from adaptive mesh refinement (AMR) cosmological simulations. They found that isothermal β model fits to X-ray surface brightness distributions of simulated clusters are biased to low β values relative to fits to SZ distributions, and that the fitted β values depend on the projected radius cut-off used. When Hallman et al. used a projected radius limit equal to $R_{\rm vir}$, the β parameters based on SZ structures scattered around $\beta = 1$. Haugbolle, Sommer-Larsen & Pedersen (2007) derived an empirical model for the pressure distribution in clusters of galaxies based on high-resolution SPH simulations and observations. They also found a steeper fall off of the pressure at large radii than that predicted by X-ray observations.

Afshordi et al. (2007) used WMAP 3 year data to stack images of 193 massive clusters of galaxies and detected the SZ effect statistically out to about 2 $R_{\rm vir}$. Using a larger cluster sample, Atrio-Barandela et al. (2008) determined the average electron pressure profile in clusters by stacking 700 known clusters extracted from the 3-year WMAP data. They showed that the isothermal β model does not provide a good fit on large scales. Both Afshordi et al. and Atrio-Barandela et al. concluded that an ICG model with a density profile with a fall off of $\rho_g \propto r^{-3}$ at large radii and a temperature profile derived from hydrostatic equilibrium is a good description of their data.

The large-scale distribution of the ICG was studied in three individual clusters of galaxies (Abell 1835, Abell 1914 and CL J1226.9+3332) by Mroczkowski et al. (2009) using SZA observations at 30 GHz (and at 90 GHz for CL J1226.9+3332). The SZA is an interferometer consisting of eight 3.5 meter diameter dishes (Muchovej et al. 2007). They used a parameterized pressure profile with five parameters based on cosmological numerical simulations of Nagai et al (2007). Mroczkowski et al. fixed the three slope parameters at their values derived from simulations and X–ray observations, and fitted only for the amplitude and the pressure scale radius using their SZ data. They used a density distribution derived from X–ray observations to determine the temperature distribution based on the ideal gas law (temperature $\propto$ pressure/density). Mroczkowski et al. (2009) found that the SZ profiles drop more steeply than predicted by isothermal β models. Their results suggest, similarly to previous studies, that the SZ profiles in clusters drop more steeply than predicted by a β model for the gas density with $\beta = 2/3$ even if the change in the temperature is taken into account (Figure 3 of Mroczkowski et al. 2009).

Vikhlinin et al. (2005) measured the temperature profile in 13 low redshift relaxed clusters using CHANDRA data. In three clusters the temperature profiles were measured out to about $0.7 R_{\rm vir}$. At $r \gtrsim 1.1 - 1.2 R_{\rm vir}$ they found that the fall off of the temperature with radius is self similar in relaxed clusters when scaled by $R_{\rm vir}$. Recently Ettori & Balestra (2009) and Bautz et al. (2009) studied the outer regions of galaxy clusters using X-ray observations. Ettori & Balestra (2009) used CHANDRA observations of 11 clusters, one pointing each, with SN ratio greater than 2 out to $r > 0.7 R_{\rm vir}$. The low count rate in the outer regions of galaxy clusters did not allow them to determine the temperature distribution out to $R_{\rm vir}$. They derived the slope of the gas density and temperature distribution at the virial radius assuming hydrostatic equilibrium. The found that the X-ray surface brightness distribution is steepening with larger radii, implying an equivalent $\beta \approx 1$ (within errors) at $R_{\rm vir}$. Bautz et al. (2009) used SUZAKU observations of relaxed cluster Abell 1795. They mapped the X-ray surface brightness and temperature distribution out to about 0.9 $R_{\rm vir}$ in two directions (North and South) using a total of 5 pointings. They found $\beta = 0.64$ within $r < 1$ Mpc. At larger radii they found a steeper fall off of the density in the South ($\beta > 0.64$), but a rising density profile towards North with a maximum at 1.9 Mpc ($1R_{\rm vir}$). The increase of the X-ray surface brightness in the North direction might be due to contribution from a filament in the LOS.

3. Models for the ICG from AMR Simulations

We derive self-similar spherically symmetric models for the distribution of the ICG in relaxed clusters of galaxies using a sample of clusters drawn from cosmological AMR simulations performed with the cosmological code ENZO (O'Shea et al. 2004) assuming a spatially flat cold DM model with cosmological parameters (Ω_m, Ω_Λ, Ω_b, h, σ_8) = (0.3, 0.7, 0.047, 0.7, 0.92), where Ω_m, Ω_b, Ω_Λ are the current matter and baryon densities and the cosmological constant in units of the critical density, σ_8 is the power spectrum normalization on 8 h^{-1} Mpc scales, and the Hubble constant $H_0 = 100$ h km s^{-1} Mpc^{-1}. This cosmological model is close to the WMAP 5 year results except for σ_8, which is much larger (Dunkley et al. 2009). The AMR simulations were adiabatic (in the sense that no heating, cooling, or feedback were included). The box size of the original, low resolution, cosmological simulation was 300 h^{-1} Mpc. The clusters of galaxies in our sample were re-simulated with high resolution using the same technique as described in Younger & Bryan (2007).

The resolutions (minimum AMR cell size) of the high-resolution simulations at $R = 0$, 1 and $4R_{\rm vir}$ were about 25 kpc, 80 kpc and 250 kpc. The total virial masses of the 10 massive clusters in our cluster sample fell between 1 and 2×10^{15} $M_\odot$. Relaxed clusters were selected based on their density distribution: after the removal of filaments, we chose clusters with a smooth spherically averaged density profile with little angular variation and no sign of recent major merger events (for more details about our simulated cluster sample and analysis see Molnar et al. 2009). In this study, for practical purposes, we also require that the density and the temperature as a function of radius increase towards the center of the cluster. Out of a total of 10 clusters, two clusters satisfy our criteria for relaxed clusters (AMRCL1 and AMRCL2). We show spherically averaged gas density and temperature profiles for our massive relaxed clusters in Figure 1 (dashed lines with error bars). The error bars represent *rms* of the density and temperature variations due to spherical averaging. While the density distributions are similar in all relaxed clusters, showing only small deviations from radial averaging, the temperature profiles show more variation. This is due to the sensitivity of the temperature to shocks from merging and internal flows. The virial shock around the nominal virial radius can be seen clearly as the radius at which the temperature profiles drop. The solid curves in Figure 1 show the density and temperature profiles for the best-fit models for AMRCL1 and AMRCL2 (see below). The physical parameters of our relaxed clusters are summarized in Table 1.

We use spherically symmetric non-isothermal β models truncated at the virial radius, $R_{\rm vir}$, to describe the density distribution of the ICG in massive relaxed clusters. We use the same functional form for the temperature distribution as Loken et al. (2002). The gas density and temperature models for massive clusters can be summarized as

$$\rho(r) \propto \ (1 + r^2/r_{\rm core}^2)^{-3\beta/2} \quad r \leq R_{vir} \ , \tag{1}$$

and

$$T(r) \propto \ (1 + r/r_{\rm T})^{-\delta} \quad r \leq R_{\rm vir} \ , \tag{2}$$

where the spatial extent is determined by the core radius, $r_{\rm core}$, and the temperature scale radius, $r_{\rm T}$; the fall off of the density and temperature profiles are determined by the parameters β and δ. These functions provide good fits to the density and temperature profiles of our relaxed clusters out to the virial radius: the fits are within the 1σ error bars due to spherical averaging, or deviate only slightly more than 1σ in a few radial points for the temperature profile (see solid lines in Figure 1). The fitted parameters, $r_{\rm core}$, β and $r_{\rm T}$ for all clusters are summarized in Table 1. Carrying out fits to the 3-dimensional (3D) temperature distribution of simulated relaxed clusters we noticed that the exponent of the temperature model, δ, does not change much from cluster to cluster (in agreement with an analysis using more clusters by Loken et al. 2002). Also, the best-fit models without fixing δ do not provide a significantly better fit than models with fixed $\delta = 1.6$, thus we fixed $\delta = 1.6$ in our fitting and in the rest of our analysis. We conclude that $\beta \approx 1$ and $\delta = 1.6$ provide good fits to our relaxed clusters. Therefore, we find that the density distribution at large radii can be approximated with a power law, $r^{-\alpha}$, with $\alpha = 3$, which is very close to $\alpha = 3.4$ found by Roncarelli et al. (2006). Our results suggest that the pressure ($\propto \rho T$), at large radii can be approximated with a power law with $\alpha = 3\beta + \delta = 4.6$, which is close to $\alpha = 5$, found by Nagai et al. (2007) and used by Mroczkowski et al. (2009). We find the density and temperature functions (Equations 1 and 2) are adequate for relaxed clusters and provide a family of ICG models that can be fitted to observational data.

4. SZ and X-ray Images of Simulated Clusters

We derive the 2-dimensional SZ and X-ray surface brightness distributions in the XY, XZ and YZ projections for our relaxed clusters. We ignore relativistic effects, which is a good approximation in our case since the intra-cluster gas temperatures in our relaxed AMR clusters is less than 10 keV. We derive the SZ signal in the XY projection by integrating along the LOS (ℓ) over the extent of the cluster (from ℓ_1 to ℓ_2) using

$$\Delta T_{CL}(x,y) = \Delta T_{CL0}\, N_{CLSZ}^{-1} \int_{\ell_1}^{\ell_2} n_e(x,y,\ell)\, T_e(x,y,\ell)\, d\ell, \tag{3}$$

where x and y are spatial coordinates in the plane of the sky, i.e. perpendicular to ℓ (which we choose to coincide with z); $n_e = f_g \rho_g / \mu_e m_P$ is the electron density, where μ_e is the mean molecular weight per electron and m_P is the proton mass; ρ_g is the gas density; f_g is the mass fraction of baryons in the cluster that are contained in the ICG (we adopt $f_g = 0.9$), and we use the standard assumption that the electron temperature equals the gas temperature, $T_e = T$. The frequency dependence is contained in $\Delta T_{CL0} = p(x_\nu)\, T_{\rm CMB}\, k_B \sigma_T/(m_e c^2)$, where the dimensionless frequency $x_\nu = h_P \nu/(k_{\rm B} T_{\rm CMB})$, where $T_{\rm CMB}$ is the monopole term of the CMB, h_P and k_B are the constants of Planck and Boltzmann, and the function $p(x_\nu) = x_\nu \coth(x_\nu/2) - 4$ (e.g., Birkinshaw 1999). The SZ normalization is

$$N_{CLSZ} = \int_{\ell_1}^{\ell_2} n_e(0,0,\ell)\, T_e(0,0,\ell)\, d\ell. \tag{4}$$

In practice, we pixelize x, y and ℓ, and approximate the integral with a sum over the LOS from $\ell_1 = -10$ Mpc to $\ell_2 = 10$ Mpc. Similar expressions were used for the XZ and YZ projections.

We include the CMB contamination in our SZ image simulations, thus we have

$$\Delta T(x,y) = \Delta T_{CL}(x,y) + \Delta T_{CMB}(x,y), \tag{5}$$

where the CMB contamination, ΔT_{CMB}, is generated as in Umetsu et al. (2004).

The Compton–y images, $y = \int d\tau\, (k_{\rm B} T_e)/(m_e c^2)$, where τ is the optical depth, the SZ images (cluster plus CMB at the AMiBA frequency band, 94 GHz), X-ray surface brightness, and simulated X-ray images including background noise, of our two relaxed clusters (AMRCL1 and 2) in the XY, XZ and YZ projections, assuming that they are located at a redshift of 0.2, are shown in Figures 2 and 3. The virial radii of our massive relaxed clusters are about 2 Mpc, which span about $10'$ on the sky at this redshift. The dark blue regions ($\approx$ -1.2mK) on the SZ images mark the cluster centers, the yellow and red regions represent positive and negative CMB fluctuations with an amplitude of about $\pm 130\,\mu$K and an *rms* of about $90\,\mu$K. In the Compton-y images we can follow the diffuse gas out to about $3R_{\rm vir}$, where the external shocks of massive clusters are found (see Molnar et al. 2009), but in the SZ images the diffuse gas around clusters seems to extend out to about $R_{\rm vir}$ only, due to contamination from CMB fluctuations, which dominate the large-scale structure. However, the SZ images of relaxed clusters, in most projections, show similar characteristics within the virial radius: a circularly-symmetric center and somewhat elongated, but still relaxed, outer regions. The core regions in the X-ray and SZ images (for example regions with yellow color in rows 1 and 3), in a few projections (XY projection of AMRCL1 and XY and YZ projections of AMRCL2), show asymmetry due to contamination by filaments in the LOS.

We derive the X-ray surface brightness in the XY projection by integrating along the LOS (ℓ) over the extent of the cluster (from ℓ_1 to ℓ_2) as

$$S_{CL}(x,y) = S_{CL0}\, N_{CLX} \int_{\ell_1}^{\ell_2} n_e^2(x,y,\ell)\, T_e^{1/2}(x,y,\ell)\, d\ell, \tag{6}$$

where S_{CL} is the central X-ray surface brightness and the normalization, N_X, is

$$N_{CLX}^{-1} = \int_{\ell_1}^{\ell_2} n_e^2(0,0,\ell)\, T_e^{1/2}(0,0,\ell)\, d\ell, \tag{7}$$

where we use the scaling $S_X \propto \sqrt{T_e}$ for thermal bremsstrahlung (similar expressions were used for the XZ and YZ projections). Similarly to the SZ surface brightness, we pixelize x, y and ℓ, and approximate the integral with a sum over the LOS from $\ell_1 = -10$ Mpc to $\ell_2 = 10$ Mpc.

We simulate X-ray images of our relaxed AMR clusters assuming a field of view of $16' \times 16'$, with a pixel size of $2'' \times 2''$. We sample the Poisson distribution with expectation values equal to the surface brightness distribution as

$$S_X(x,y) = S_{CL}(x,y) + B_X, \tag{8}$$

where we calculate $S_{CL}(x,y)$ using Equation 6 assuming $S_{CL0} = 6$ cnts/pixel and a uniform background of $B_X = 0.2$ cnts/pixel (typical parameters for X-ray observations of clusters of galaxies). We show the X-ray surface brightness distribution in relaxed clusters and their simulated X-ray images including background noise in Figures 2 and 3 (third and fourth rows, logarithmic scale).

5. AMiBA13 Visibility Simulations

Interferometers measure visibilities, the Fourier transforms of the intensity distribution multiplied by the primary beam of the telescope. In the small-angle approximation, the visibilities can be written as

$$V_\nu(u,v) = \int_{-\infty}^{\infty}\int_{-\infty}^{\infty} B_\nu(x,y)\, I_\nu(x,y)\, e^{-i2\pi(ux+vy)}\, dx\, dy, \tag{9}$$

where $V_\nu(u,v)$ is the visibility function in the uv plane, which is the Fourier conjugate of the positions, x and y on the sky; $B_\nu(x,y)$ and $I_\nu(x,y)$ are the primary telescope beam pattern and source intensity at x and y at the observational frequency ν. We convert temperature differences to intensity units using

$$\frac{\Delta I}{I_{\rm CMB}} = \frac{x_\nu^4\, e^{x_\nu}}{(e^{x_\nu}-1)^2}\, \frac{\Delta T}{T_{\rm CMB}}, \tag{10}$$

where $I_{\rm CMB}$ is the intensity of the monopole term in the CMB. The visibilities, $V_{\rm CL}$ and $V_{\rm CMB}$ at frequency ν are calculated from $\Delta T_{\rm CMB}$ and $\Delta T_{\rm CL}$ using Equations 9 and 10, and we ignore the monopole term since interferometers are sensitive only to intensity differences.

We simulated visibilities for mock two-patch AMiBA13 observations of our relaxed clusters assuming a compact configuration for the 13 antennas (Figure 4; for a detailed description see Koch et al., in preparation). The advantage of this configuration is that the many short baselines provide high sensitivity to the large-scale distribution of the radio signal. The instrument noise and the contribution from the CMB were simulated in visibility space and added to the visibilities of the simulated clusters (see Umetsu et al. 2004). We assumed an observing time of 120 hours on-source. The errors in the azimuthally averaged visibilities for the simulated clusters, for the CMB and for the instrument noise are all comparable at this exposure time. Using longer exposure would reduce the errors for the instrument noise, but would not lower the errors either for our ICG models or for the CMB. Therefore we would not be able to reduce the error bars significantly by using longer observations. Usually a subtraction scheme is used in cluster SZ observation with half of the time on-source, and half of the time off source to reduce systematics, ground pick up and sky background (e.g., Wu et al. 2009). Therefore 120 hrs of on-source integration involve 240 hr of total observing time. This can be conveniently accommodated into a 1-month observing schedule.

We use only projections of relaxed clusters which are not contaminated by filaments in the LOS (XZ and YZ projection of AMRCL1 and XZ projection of AMRCL2). We derive simulated visibilities for two-patch observations as

$$V(u_i, v_i) = V_{source}(u_i, v_i) - V_{bkng}(u_i, v_i), \tag{11}$$

where the on-source visibilities, $V_{\rm source}$, are

$$V_{\rm source}(u_i, v_i) = V_{\rm CL}(u_i, v_i) + V_{\rm CMB}(u_i, v_i) + V_{\rm noise}(u_i, v_i), \tag{12}$$

and the off-source (background) visibilities, $V_{\rm bknd}$, are

$$V_{\rm bknd}(u_i, v_i) = V'_{\rm CMB}(u_i, v_i) + V'_{\rm noise}(u_i, v_i), \tag{13}$$

where $V_{\rm SZ}$ is the visibility of the SZ signal, $V_{\rm CMB}$, $V_{\rm noise}$, and $V'_{\rm CMB}$, $V'_{\rm noise}$ are two sets of visibilities of the CMB fluctuations and noise (different for on- and off-source observations). We assumed that the CMB fluctuation fields for the two patches (about one degree apart) are uncorrelated, which is a conservative assumption: this way we somewhat overestimate the noise due to the CMB. Since our models are spherically symmetric, we have no constraints on them from the imaginary part of the model visibilities (the imaginary part is identically zero), therefore we work only with the real part of the visibilities. Note that in real applications the imaginary parts can be used to check the amplitude of the CMB fluctuations in the field, assess non-sphericity of the cluster and the pointing accuracy. As an illustration, in Figure 5 we show the radial profile of the real part, $\mathcal{R}e(V)$, of the azimuthally averaged simulated visibilities of one realization of a two-patch observation for AMRCL1 in Projection XY for the 90 and 98 GHz AMiBA channels (Channels A and B, Ho et al. 2009) as a function of R_{uv}. Since the length scale for the visibility data is in units of the observing wavelength, the visibilities are represented by two sets of curves. The red diamonds and green squares with error bars represent visibilities for Channel A and B. The error bars represent the *rms* of the azimuthally averaged real part of the visibilities at the AMiBA13 baselines. As a comparison, black plus signs and crosses with error bars show azimuthally averaged visibilities of AMiBA observations in the first configuration, AMiBA7 (assuming the same exposure time, 120 hours as before). Visibilities of other projections for AMRCL1 and projections of AMRCL2 with no contamination from filaments are very similar due to the structural similarity among the cluster SZ images in these projections (see Figures 2 and 3).

6. Model Fitting

We use non-isothermal β models truncated at the virial radius for the ICG. We determine the best-fit parameters using likelihood functions. The SZ surface brightness distributions based on our models (Equations 1 and 2) have six free parameters: five shape parameters, $p = (r_{\rm core}, \beta, r_{\rm T}, \delta, R_{\rm vir})$, and one amplitude, ΔT_0. Unfortunately, due to limited spatial resolution, field of view and receiver noise, we do not expect to be able to determine all six parameters using AMiBA13. Thus, similarly to Mroczkowski et al. (2009), we reduce the number of free parameters in our models. We proceed the following way: we determine the density shape parameters, $r_{\rm core}$ and β, from the simulated X-ray images and use simulated AMiBA13 visibilities and results based on our numerical simulations of clusters to constrain the shape parameters, $r_{\rm T}$ and δ, of the temperature distribution.

As a first step, we determine $r_{\rm core}$ and β from simulated X-ray observations. The X-ray surface brightness distribution based on our models can be calculated as

$$S_{CLM}(x, y, p) = S_0 \, N_X \, \mathcal{I}_X(x, y, p), \tag{14}$$

where S_0 is the X-ray central surface brightness, the normalization is $N_X^{-1} = \mathcal{I}_X(0, 0, p)$, and

$$\mathcal{I}_X(x, y, p) = 2 \int_0^{\ell_c} (1 + r^2/{r_{\rm core}}^2)^{-3\beta} \, (1 + r/r_T)^{-\delta/2} d\ell, \tag{15}$$

where $r^2 = x^2 + y^2 + \ell^2$, and the cut off in the LOS is $\ell_c^2 = R_{\rm vir}^2 - x^2 - y^2$. Note, that since $r/r_{\rm core}$ and r/r_T are both dimensionless, $S_{CLM}(x, y, p)$ depends on $R_{\rm vir}$ only through the cut off, ℓ_c. X-ray observations detect individual photons, which have a Poisson distribution. We experimented with the likelihood ratio for Poisson distribution, χ_r^2, and Mighell's χ_γ^2 statistic (see Mighell 1999 for a detailed analysis) in fitting this structure. We found that the fitted parameters obtained by these two methods are virtually identical. Therefore we decided to use the likelihood ratio test:

$$-2 \, \ln \mathcal{L}_X = \chi_r^2 = \sum_i M_i - N_i + N_i \, \ln(N_i/M_i), \tag{16}$$

where N_i and M_i are the observed and expected numbers of photons.

Since the shape parameters are not too sensitive to the large-scale distribution of the temperature (heavily weighted towards the center of the cluster), we determine $r_{\rm core}$ and β using isothermal β model fits to our simulated X-ray surface brightness maps. In this case, since $\beta \approx 1$ (see Table 1), the X-ray emissivity, which is proportional to $(1 + r^2/{r_{\rm core}}^2)^{-3}$, drops about 6 orders of magnitude from the cluster center to the virial radius. Therefore a reasonable change in $R_{\rm vir}$ (say 20%) causes only an insignificant change in the X-ray signal (Equation 15) due to a change in the upper limit, ℓ_c (except around $R_{\rm vir}$ where the X-ray signal is negligible; see Figures 2 and 3). For our purposes, therefore, we fix the value of $R_{\rm vir}$ assuming that an estimate for its value with a 20% accuracy is available from other measurements. We determined $r_{\rm core}$, β by minimizing the X-ray likelihood function, Equation 16, with the shape parameter, $p = (r_{\rm core}, \beta, \infty, 0, R_{\rm vir})$. In Figures 6 and 7 we show the confidence limits (CLs) of the X-ray likelihood functions of fitting isothermal β models to the XZ and YZ projection of AMRCL1 (blue dashed, and green dot-dashed lines), and the XZ projection of AMRCL2 (red dashed lines). We also show the the CLs for fitting to the 3D density distribution of AMRCL1 and AMRCL2 (black contours).

We conclude from these figures that the fits are biased toward lower $r_{\rm core}$ and β values. We obtain better estimates of the core radii if we fix $\beta = 1$. Note that non-isothermal β model fits return an even lower β, so taking into account the temperature distribution will cause even stronger bias towards lower $r_{\rm core}$ and β values. In the following analysis we assume $r_{\rm core}$ is as determined from our X-ray fits and use $r_{\rm core}$ and $\beta = 1$.

We calculate the visibilities for our models, V_M, at frequency ν, using Equations 9 and 10, as

$$\Delta T_{CLM}(x, y) = \Delta T_0 \, N_{SZ} \, \mathcal{I}_{SZ} \, (x, y, p), \tag{17}$$

where ΔT_0 is the central SZ amplitude, the normalization is $N_{SZ}^{-1} = \mathcal{I}_{SZ}(0, 0, p)$, and

$$\mathcal{I}_{SZ}(x, y, p) = 2 \int_0^{\ell_c} (1 + r^2/{r_{\rm core}}^2)^{-3\beta/2} \, (1 + r/r_T)^{-\delta} d\ell. \tag{18}$$

Note, that since $r/r_{\rm core}$ and r/r_T are both dimensionless, $\Delta T_{CLM}(x, y)$ depends on $R_{\rm vir}$ only through ℓ_c.

We determine the best fit parameters for our models by maximizing the SZ likelihood function defined as

$$-2 \, \ln \mathcal{L}_{SZ} = \sum_{i,j} \frac{[\mathcal{R}e\{V_O(R_{uv}^i; \nu_j)\} - \mathcal{R}e\{V_M(R_{uv}^i; \nu_j)\}]^2}{\sigma_{ij}^2}, \tag{19}$$

where $\mathcal{R}e\{V_O\}$ and $\mathcal{R}e\{V_M\}$ are the azimuthally averaged real part of the observed and model visibilities at the ith uv radius, R_{uv}^i, at frequency ν_j, where $j = 1, 2$ for the two

AMiBA frequency channels, and σ_{ij} is the Gaussian noise assumed to be the same for all antenna pairs and frequencies.

We assume that $r_{\rm core}$ is known from X-ray data analysis, $\beta = 1$, $\delta = 1.6$, from numerical simulations, and that $R_{\rm vir}$ is available from other measurements. Again, similarly to the X-ray signal, a reasonable change in $R_{\rm vir}$ (all the other parameters fixed) causes only an insignificant change in the SZ signal (Equation 18) because, in our models, $\beta \approx 1$ and $\delta \approx 1.6$, therefore the pressure is about four orders of magnitude smaller at the virial radius than at the center of the cluster. Therefore the shape parameter in our case, $p = (r_{\rm core}, 1, r_{\rm T}, 1.6, R_{\rm vir})$, with one unknown: $r_{\rm T}$. We determine the best fit for $r_{\rm T}$ by maximizing the SZ likelihood function, Equation 19. In Figures 8 and 9 we show the CLs of the likelihood function as a function of $r_{\rm T}$. In Figure 8, the blue dashed and green dot-dashed lines show likelihood functions for fits in the XZ and YZ projections of AMRCL1. The red dashed line in Figure 9 represents the likelihood function for fits in the XZ projection of AMRCL2.

7. Discussion

We simulated AMiBA13 observations of massive relaxed clusters of galaxies including CMB contamination and receiver noise using clusters drawn from cosmological numerical simulations to assess how well we should be able to constrain the large-scale distribution of the ICG with AMiBA13. Based on our simulated SZ images (rows 2 in Figures 2 and 3), we conclude that, at 94 GHz, on the scale of the cluster cores (few arc minutes), the cluster SZ signal dominates the CMB fluctuations, so that CMB contamination is not important in surveys for rich clusters. On a scale of ten arc minute, corresponding to the extent of the ICG in massive clusters, however, CMB contamination is at a comparable level to the SZ signal. This suggests that the separation of the cluster SZ and the CMB signals is essential for studying the SZ signature of the large-scale structure. Contamination from CMB fluctuations is also important in the regions in galaxy clusters close to their virial radius.

We can assess the improvement due to upgrading the first AMiBA configuration, AMiBA7 (7 dishes with 60 cm in diameter) to AMiBA13, which consists of 13 dishes with 120 cm in diameter, by inspecting Figure 5. We have 6 R_{uv} points for each of the two AMiBA channels (a total of 12 points) as opposed to the 3 R_{uv} points per channel (a total of 6) in the current configuration. 3 R_{uv} points per channel is not sufficient to put meaningful constraints on the shape parameters, $r_{\rm core}$ and β. Although AMiBA with the first configuration can measure visibilities at uv radius about 200 where the signal is about a factor of two larger than it is at the smallest R_{uv} of about 350 for AMiBA13 (note, that due to the finite size of the antennas, R_{uv} cannot be smaller than the diameter of the antennas expressed in units of the observing wavelength), this reduction of the signal is compensated by the smaller error bars for AMiBA13 (±0.0025 Jy *vs.* ±0.013 Jy for the shortest baselines assuming the same exposure time). The error bars are reduced for AMiBA13 because of two reasons: i) larger collecting areas of the antennas (diameter of 120 cm *vs.* 60 cm); ii) more baselines providing more measurements with the same R_{uv}. AMiBA13 is a unique interferometer. In its frequency range, 94 GHz, it has the shortest baselines corresponding to $R_{uv} = 400$, among presently operating interferometers. The shortest baseline of the SZA interferometer for example at 90 GHz is about 1000. Note, that at this frequency, the cluster SZ signal is about eight times larger at $R_{uv} = 400$ than at $R_{uv} = 1000$ (see Figure 5).

Using our AMR simulations, we showed that non-isothermal β models with a temperature distribution described by Equation 2 provide good fits to the large-scale distribution of the ICG in relaxed massive clusters. We used these models to fit to simulated X-ray and visibility (AMiBA13) data.

We generated X-ray and SZ images of our relaxed clusters drawn from numerical simulations assuming the clusters are at a redshift of 0.2. We used the simulated X-ray data to determine the shape parameters, $r_{\rm core}$, β, of the density distribution. We minimized the X-ray likelihood function (Equation 16), and determined the confidence levels using Monte Carlo simulations. From the confidence levels for our fits to the X-ray data (Figures 6 and 7), we notice a degeneracy between the two shape parameters of the β model: $r_{\rm core}$ and β. Each combination: small $r_{\rm core}$, β and large $r_{\rm core}$, β, gives a good fit to the simulated observations. A similar degeneracy has been reported for fitting β models to actual X-ray observations (e.g., Grego et al. 2001; Reese et al. 2000). We also notice that the values of $r_{\rm core}$ and β are systematically lower than what we would expect based on direct fits to the 3D density distribution. We tried to use different values for the central X-ray amplitude (S_{CL0}) and background (B_X), in our X-ray simulations, but found that only the confidence levels change, the fitted values remain the same. We concluded that this bias is systematic. From these figures we can see that if we fix $\beta = 1$, we get a much better approximation to the "real" value of $r_{\rm core}$ (the value we obtained by fitting a β model directly to the 3D density distribution in relaxed clusters; see Table 1).

Thus, we determine $r_{\rm core}$ from fitting to simulated X-ray data assuming that $\beta = 1$. We also fix $\delta = 1.6$ and assume that $R_{\rm vir}$ is known from other measurements. Then we used simulated AMiBA13 visibilities to determine the temperature scale radius, $r_{\rm T}$, by minimizing the SZ likelihood function (Equation 19), and determined the confidence levels from Monte Carlo simulations. We show the results in Figures 8 and 9. In the XZ and YZ projections in AMRCL1, we obtain $r_T = 1.8^{+0.7}_{-0.5}\ R_{\rm vir}$ (68% CL, statistical), in both projections, which is about twice the value of the fit directly to the 3D temperature distribution (Table 1). Fitting our models to simulated AMiBA13 visibilities based on spherically symmetric cluster gas models show no bias in the fitted parameters, therefore we conclude that the bias we found fitting to visibilities based on our simulated clusters is probably due to modeling, in particular, the usage of spherically symmetric models. This bias could also be caused by deviations from our density and temperature models. Slight deviations from our best fit density and temperature models do exist close to $R_{\rm vir}$ (see Figure 1), but AMiBA13 is not sensitive to the low signal originating from the the vicinity of $R_{\rm vir}$. In the XZ projection of AMRCL2 we get $r_T = 0.8^{+0.4}_{-0.25}\ R_{\rm vir}$ (68% CL, statistical), which is close to the value we obtain by fitting directly to the 3D temperature distribution (Table 1). We found no bias in $r_{\rm T}$ in this case.

We carried out simulations at different redshifts between 0.1 and 0.4. For a distant cluster the beam dilution reduces the signal; if the cluster is too close, the outer parts of the cluster fall outside of the field of view. We have found that the optimal redshift for determining the large-scale distribution of the ICG with AMiBA13 is $z \approx 0.2$.

We conclude that we should be able to use AMiBA13 to determine the large-scale distribution of the ICG in massive relaxed clusters of galaxies located at a redshift of 0.2 by determining the temperature scale radius with an about 50% statistical accuracy. In summary, our results suggest that AMiBA, once upgraded to 13 dishes with 1.2-m in diameter, will be a powerful tool for constraining the large-scale distribution of the ICG.

In this paper we considered spherically symmetric galaxy cluster models, and focused on statistical errors due to the AMiBA13 telescope and receiver system, but found that the systematic errors due to modeling could be much larger (50% *vs.* a factor of two). We expect that improving on our ICG models, i.e., using non-spherically symmetric models, would reduce the bias in the fitted parameters. Also, we should be able to reduce the necessary observation time with a more sophisticated observational strategy. A single pointing to the center of the cluster, although it simplifies the data analysis, has the disadvantage that it has a reduced sensitivity at the outer parts of the cluster, where the signal is weaker. These two effects reduce the signal to noise ratio to a low value at the outer part of the cluster. We expect that mosaic observations including pointings towards the outer regions in clusters, although more difficult to analyze, would enable us to reach our goal with an exposure time shorter than 120 hrs. We leave simulations to quantify the effects of mosaic observations and more sophisticated ICG models for future work.

Our special thanks go the the AMiBA team for their many years of dedicated work which made this project possible. KU is partially supported by the National Science Council of Taiwan under the grant NSC97-2112-M-001-020-MY3. MB acknowledges support from the STFC. GB acknowledges support from NSF grants AST-05-07161, AST-05-47823 and supercomputing resources from the National Center for Supercomputing Applications. ZH was supported by the NSF grant AST-05-07161 and by the Polányi Program of the Hungarian National Office for Research and Technology (NKTH). NH acknowledges support from the ASC Academic Alliances Flash Center at the University of Chicago, which is supported in part by the U.S. Department of Energy, contract B523820.

REFERENCES

Allen, S. W., Schmidt, R. W., Ebeling, H., Fabian, A. C., & van Speybroeck, L. 2004, MNRAS, 353, 457

Afshordi, N, Lin, Y. T., Nagai, D., & Sanderson, A. J. R. 2007, MNRAS, 378, 293

Atrio-Barandela, F., Kashlinsky, A., Kocevski, D., & Ebeling, H. 2008, ApJ, 675, L57

Bautz, M. W., et al, 2009, arXiv:0906.3515

Birkinshaw, M. 1999, Phys. Rept., 310, 97

Borgani, S. 2006, arXiv:0605575

Bryan, G.L., & Norman, M.L. 1998, ApJ, 495, 80

Carlstrom, J. E., Holder, G. P., & Reese, E. D. 2002, ARA&A, 40, 643

Cavaliere, A., & Fusco-Femiano, R., 1976, A&A, 49, 137

Chen, M.-T., et al. 2009, ApJ, 694, 1664

Dunkley, J., et al. 2009, ApJS, 180, 306

Ettori, S. 2004, Ap&SS, 290, 177

Ettori, S. & Balestra, I. 2009, A&A, 496, 343

Fang, W., & Haiman, Z. 2008, ApJ, 680, 200

Grego, L., Carlstrom, J. E., Reese, E. D., Holder, G. P., Holzapfel, W. L., Joy, M. K., Mohr, J. J., & Patel, S. 2001, ApJ, 552, 2

Haiman, Z., Mohr, J. J., & Holder, G. P. 2001, ApJ, 553, 545

Hallman, E. J., Burns, J. O., Motl, P. M., & Norman, M. L. 2007, ApJ, 665, 911

Haugbolle, T., Sommer-Larsen, J., & Pedersen, K., 2007, arXiv:0712.2453v1

Henry J. P. 2000, ApJ, 534, 565

Ho, P. T. P., et al. 2009, ApJ, 694, 1610

Holder, G., Haiman, Z., & Mohr, J. J. 2001, ApJ, 560, L111

Huang, C.-W. L. et al. 2009, ApJ, submitted

Koch, P. M., et al. 2009a, ApJ, 694, 1670

Koch, P. M., et al. 2009b, ApJ, submitted

Lin, K.-Y., et al. 2009, ApJ, 694, 1629

Liu, G. C., et al. 2009, ApJ, submitted

Loken, C., Norman, M. L., Nelson, E., Burns, J., Bryan, G. L., & Motl, P. 2002, ApJ, 579, 571

Maughan, B. J., Jones, C., Forman, W., & Van Speybroeck, L. 2008, ApJS, 174, 117

Mighell, K., J., 1999, ApJ, 518, 380

Molnar, S. M., Birkinshaw, M., & Mushotzky, R. F. 2002, ApJ, 570, 1

Molnar, S. M., Haiman, Z., Birkinshaw, M., & Mushotzky, R. F. 2004, ApJ, 601, 22

Molnar, S. M., Hearn, N., Haiman, Z., Bryan, G., Evrard, A., & Lake, G. 2009, ApJ, 696, 1640

Mroczkowski, T., et al. 2009, ApJ, 694, 1034

Muchovej, S., et al. 2007, ApJ, 663, 708

Nagai, D., Kravtsov, A. V., & Vikhlinin, A. 2007, ApJ, 668, 1

Nishioka, H., et al. 2009, ApJ, 694, 1637

O'Shea, B.W., Bryan, G. L., Bordner, J., Norman, M. L., Abel, T., Harkness, R., & Kritsuk, A. 2004, arXiv:0403044

Reese, E. D., et al. 2000, ApJ, 533, 38

Rephaeli, Y. 1995, ARA&A, 33, 541

Roncarelli, M., Ettori, S., Dolag, K., Moscardini, L., Borgani, S., & Murante, G. 2006, MNRAS, 373, 1339

Sarazin, C. L., 1988, Cambridge Astrophysics Series, Cambridge: Cambridge University Press, 1988

Sunyaev, R. A., & Zel'dovich, Ya. B. 1980, ARA&A, 18, 537

Umetsu, K., Chiueh, T., Lin, K.-Y., Wu, J.-M., & Tseng, Y.-H. 2004, Modern Physics Letters A, 19, 1027 (arXiv:0402009)

Umetsu, K., et al. 2009, ApJ, 694, 1643

Vikhlinin, A., Markevitch, M., Murray, S. S., Jones, C., Forman, W., & Van Speybroeck, L. 2005, ApJ, 628, 655

Voit, G. M. 2005, Reviews of Modern Physics, 77 207

Vikhlinin, A., et al. 2008, arXiv:0812.2720

Wu, J.-H. P., et al. 2009, ApJ, 694, 1619

Younger, J. D., & Bryan, G. L. 2007, ApJ, 666, 647

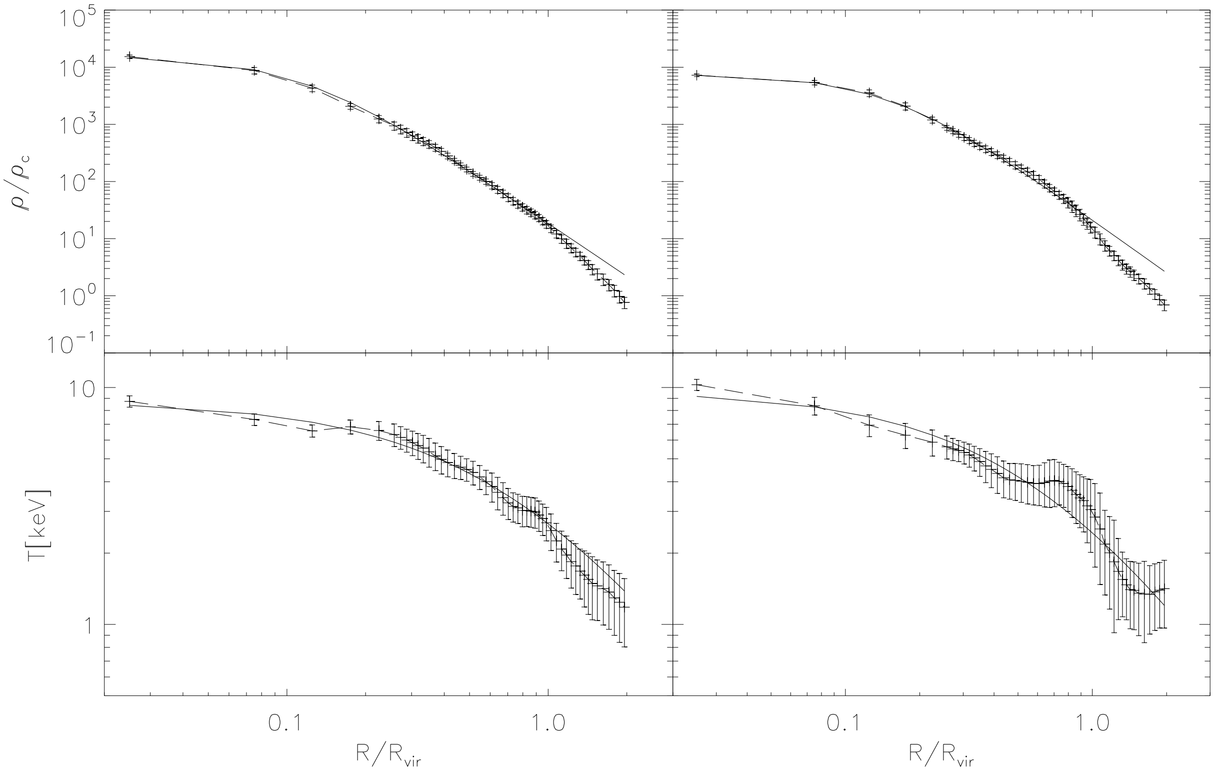

Fig. 1.— Spherically averaged gas density, ρ, (in units of the critical density, ρ_c) and temperature, T (in keV) distributions of the relaxed massive clusters AMRCL1 (left panel) and AMRCL2 (right panel) as a function of radius in units of the virial radius, $R_{\rm vir}$ (dashed lines). The error bars represent *rms* variations due to spherical averaging. The solid lines show the best-fit density and temperature models (extended out to 2 $R_{\rm vir}$ to show the deviations outside of the virial radius).

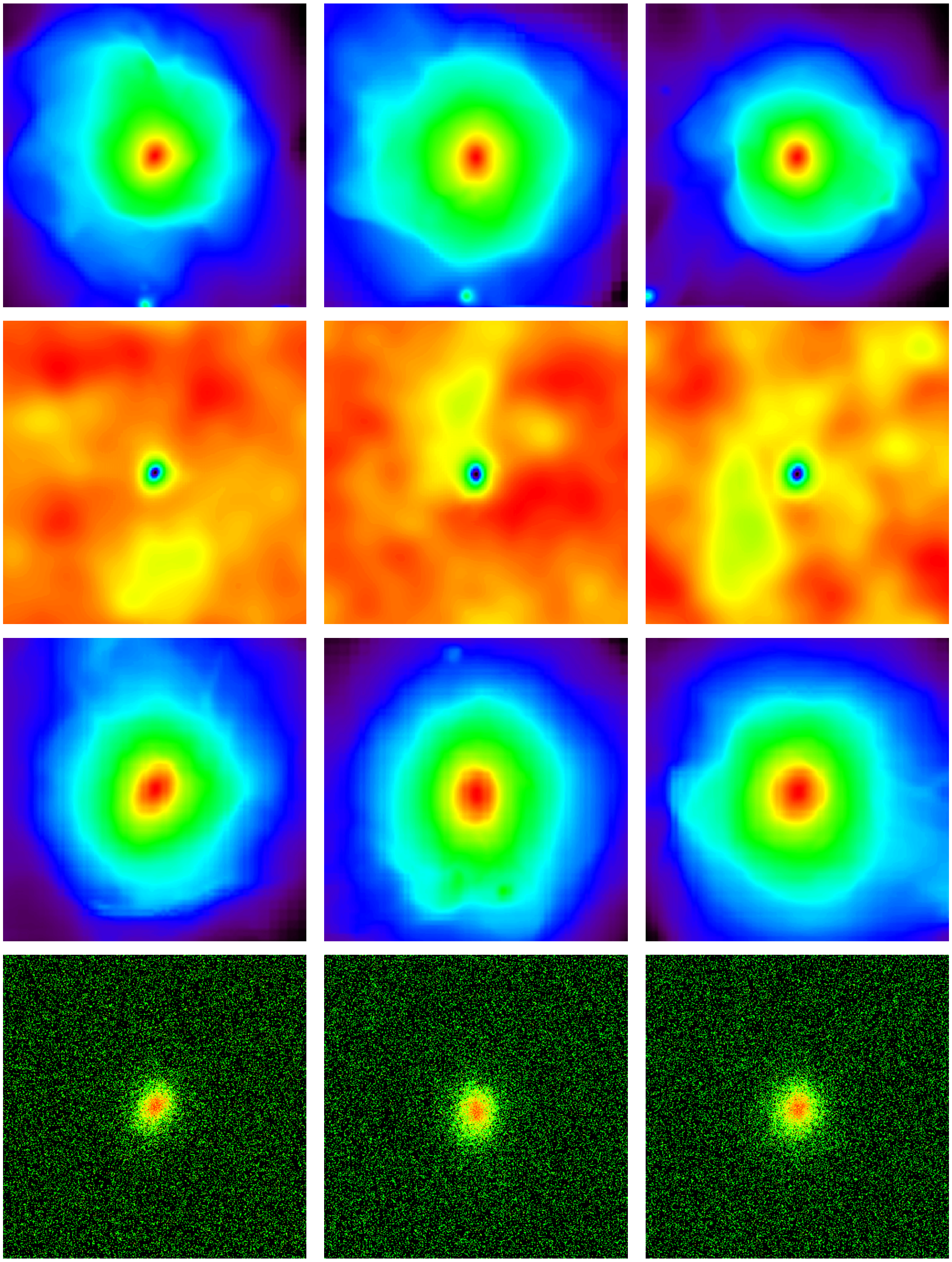

Fig. 2.— XY, XZ, and YZ projections (left, middle and right column) of relaxed cluster AMRCL1. From top to bottom: Compton-y, ΔT (including the cluster SZ signal and CMB fluctuations at 94 GHz), X-ray surface brightness and simulated X-ray image including background noise (logarithmic color scale except SZ map which is linear). The image size is $60' \times 60'$ for the SZ images (first two rows) and $16' \times 16'$ for the X-ray images (last two rows).

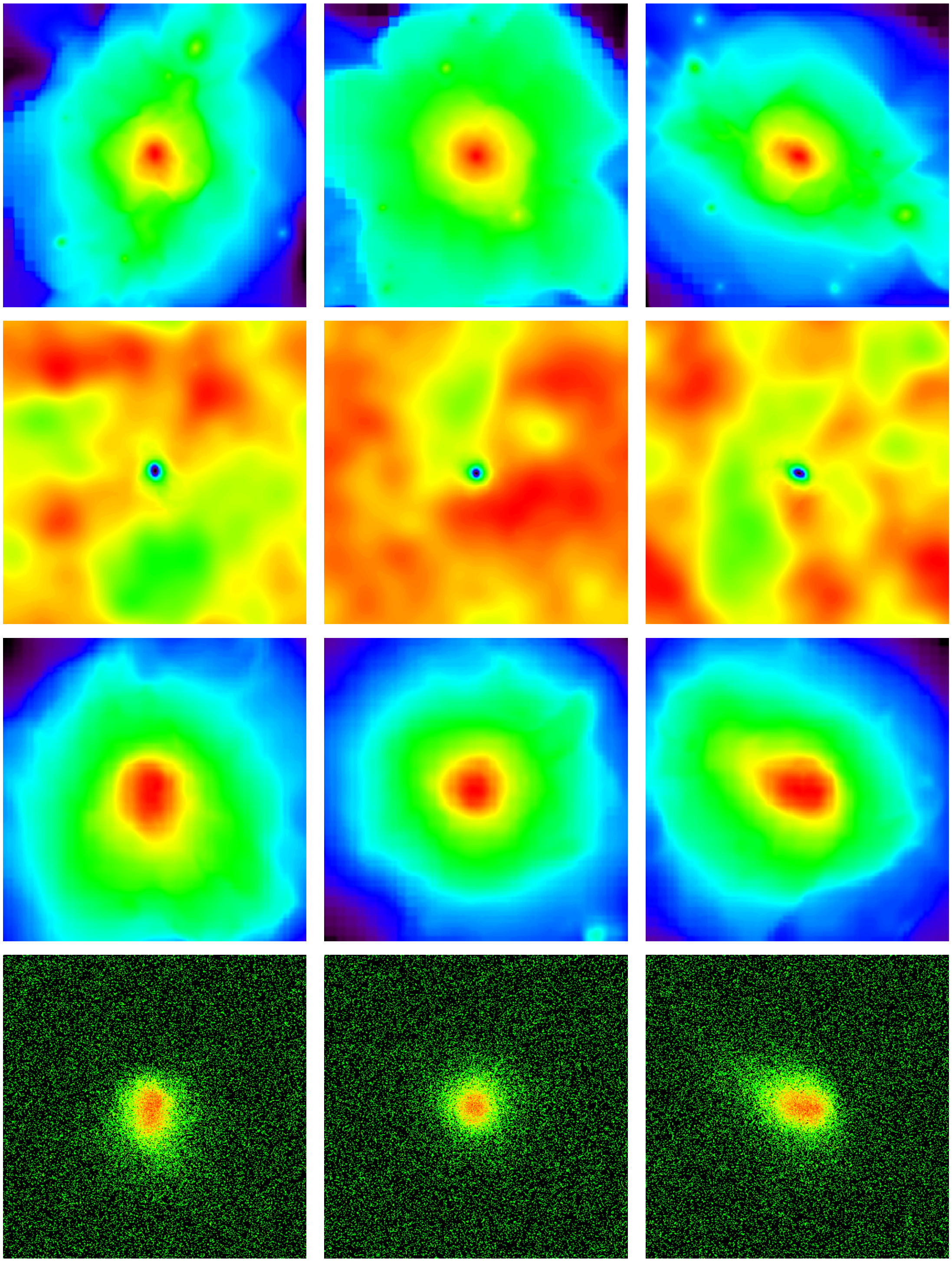

Fig. 3.— Same as Figure 2 but for the XY, XZ, and YZ projections of relaxed cluster AMRCL2.

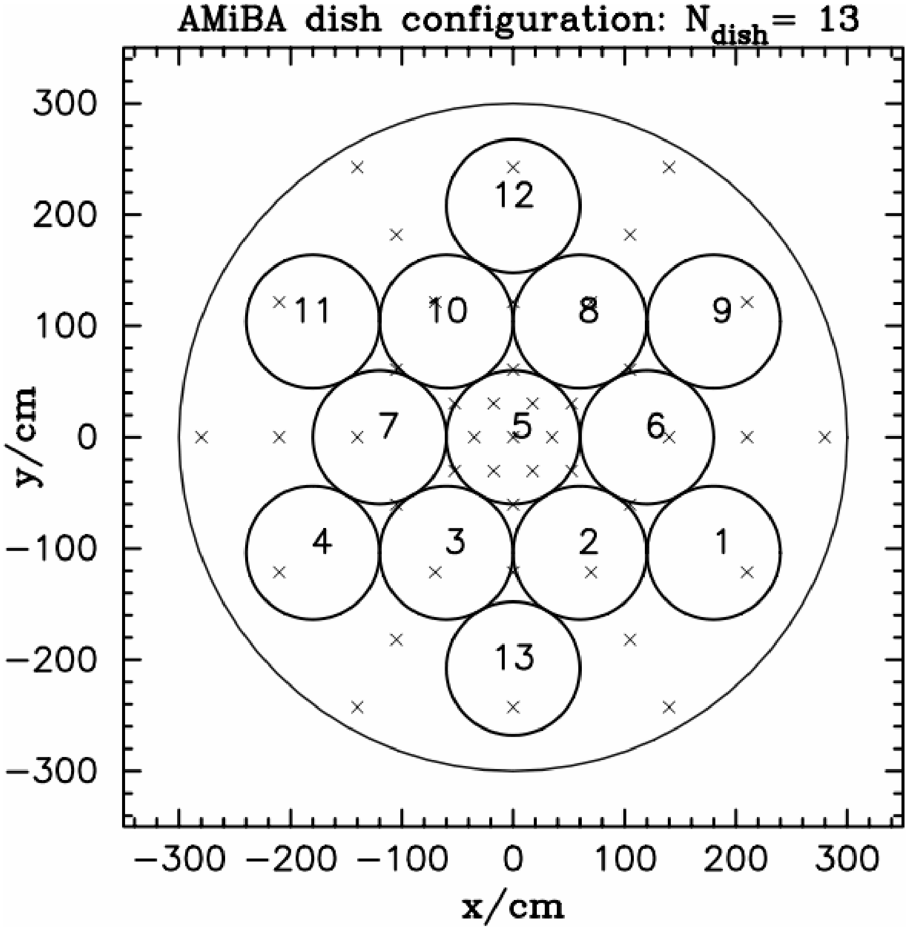

Fig. 4.— Planned antenna layout for AMiBA13 in the compact configuration (13 dishes with 1.2 m diameter) used for simulations in this paper. Additional possible antenna positions are marked with ×-s.

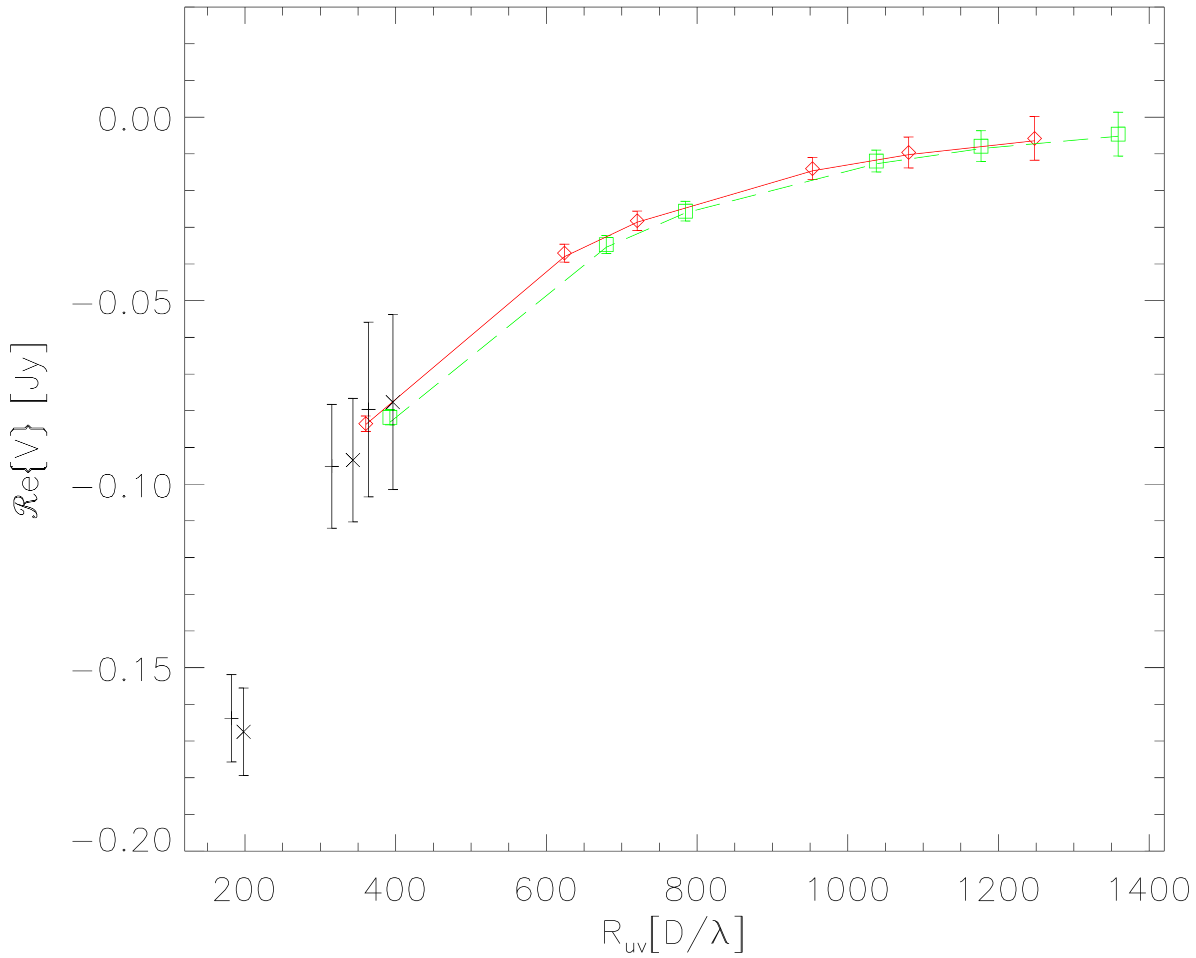

Fig. 5.— Real part, $\mathcal{R}e\,\{V\}$ (in Jy), of the azimuthally averaged simulated visibilities as a function of uv radius (R_{uv}) of the XZ projection of the AMRCL1 (plus CMB and noise, one realization) for AMiBA13 Channel A and B (red diamonds and green squares) in a compact configuration (see Figure 4). The error bars represent instrumental errors of 120 hour observations. The best-fit β model is also shown for the two channels (solid red and dashed green lines). Black points marked with plus signs and crosses with larger black error bars illustrate visibilities assuming the previous configuration for AMiBA (7 elements, 0.6 cm dishes) and the same exposure time as above.

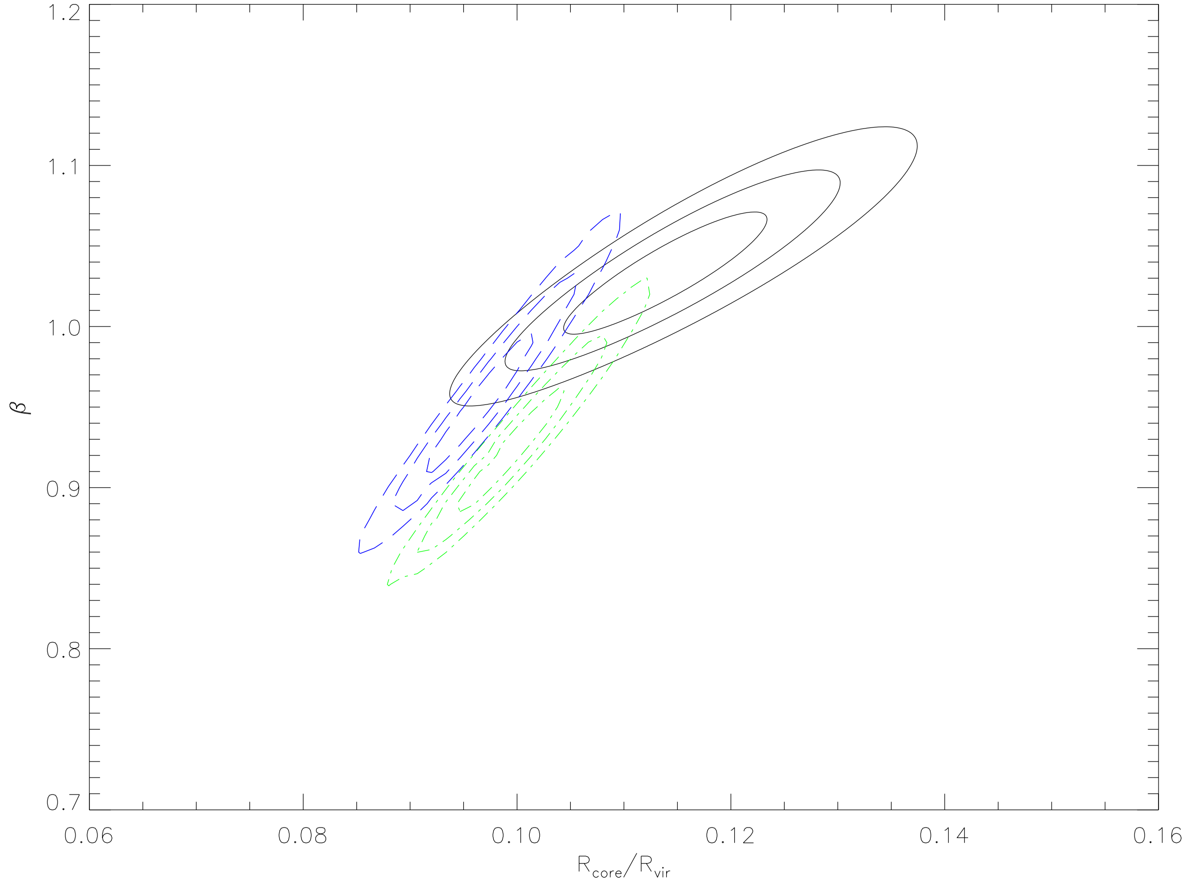

Fig. 6.— Likelihood contours (68%, 95.4% and 99.7% CLs determined from Monte Carlo simulations) for fitting β models to the relaxed cluster AMRCL1. The solid black lines represent CLs for β model fits to the 3D density distribution, the dashed blue and dot-dashed green lines represent CLs for fits to the XZ and YZ projections of the simulated X-ray image using isothermal β models.

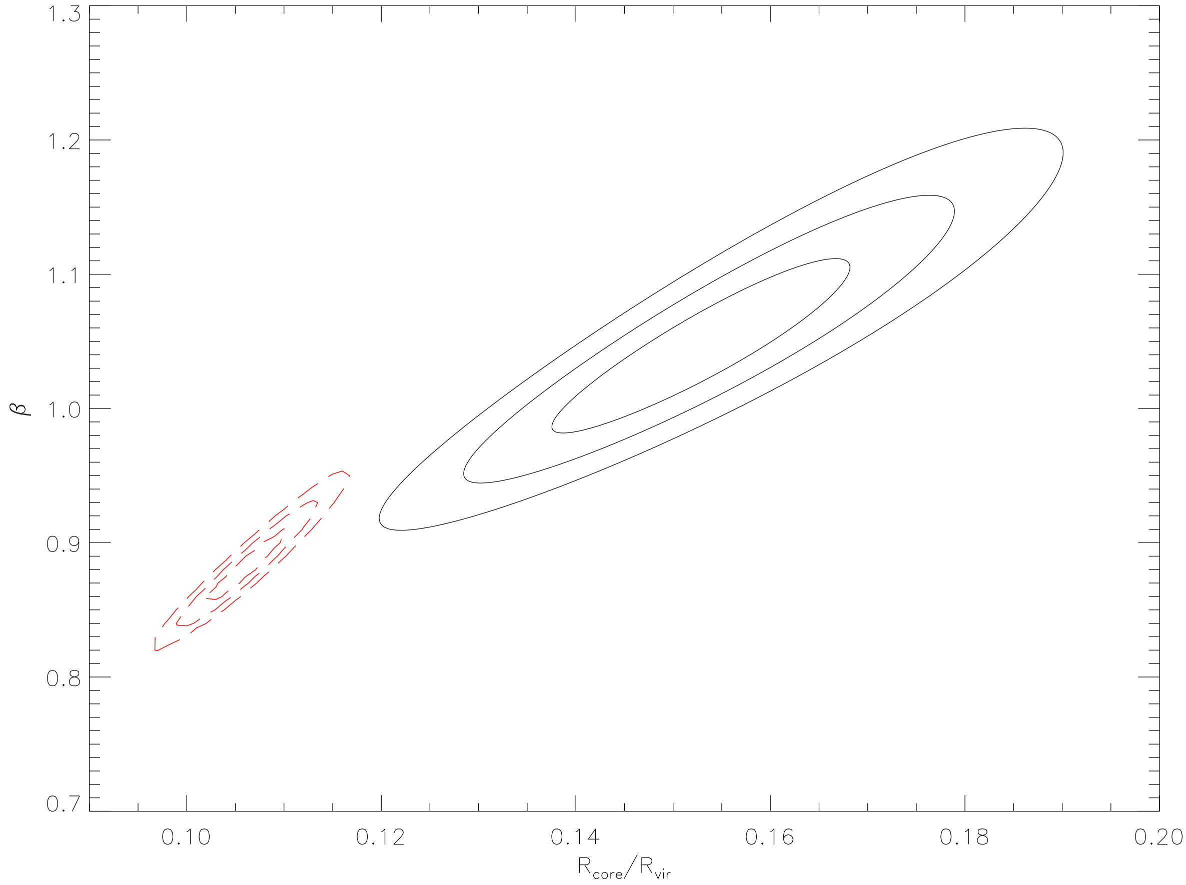

Fig. 7.— Same as Figure 6 but for the relaxed cluster AMRCL2. The solid black lines represent fits to the 3D density distribution and the red dashed lines represent CLs for fits to the XZ projection of the simulated X-ray image using isothermal β models.

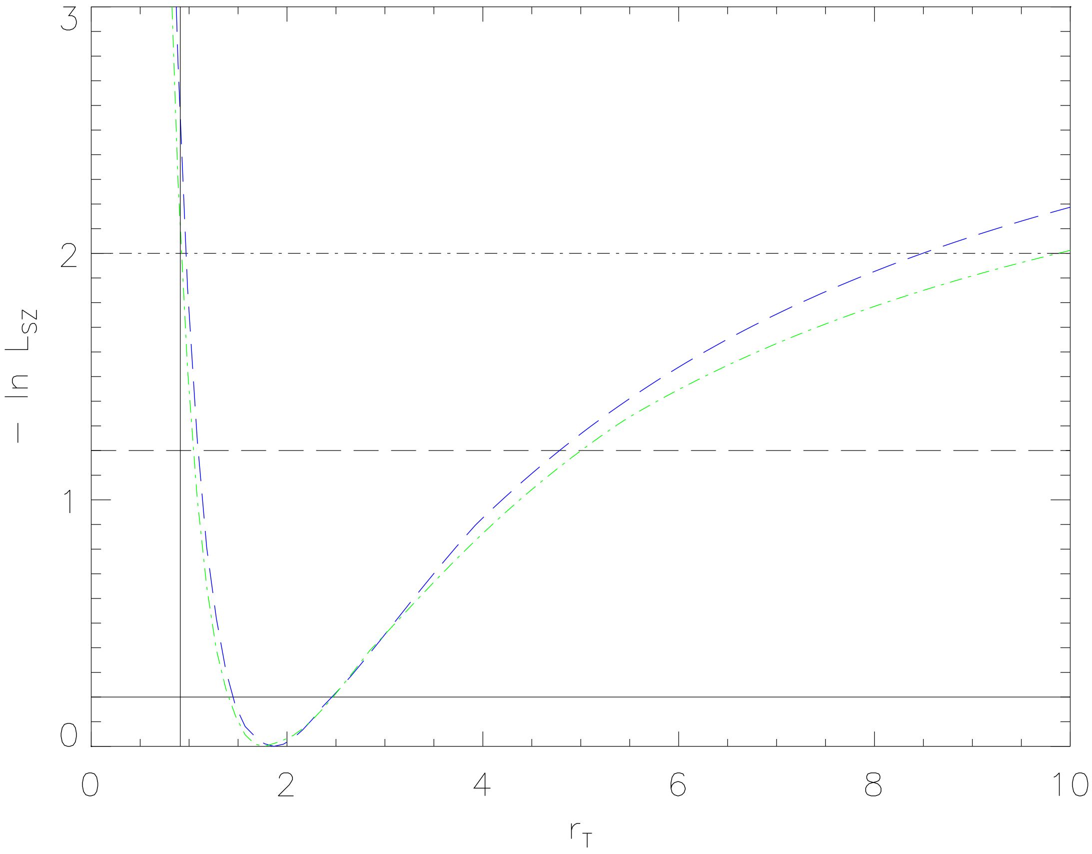

Fig. 8.— Likelihood contours for fitting temperature models to the SZ image of relaxed cluster AMRCL1 in the XZ and YZ projections as a function of $r_{\rm T}$ in units of $R_{\rm vir}$ (green dot-dashed and blue dashed lines). The solid, dashed and dot-dashed horizontal lines represent 68%, 95.4% and 99.7% CLs. The vertical solid line shows the best-fit value of $r_{\rm T}$ obtained by fitting directly to the temperature profile of AMRC1.

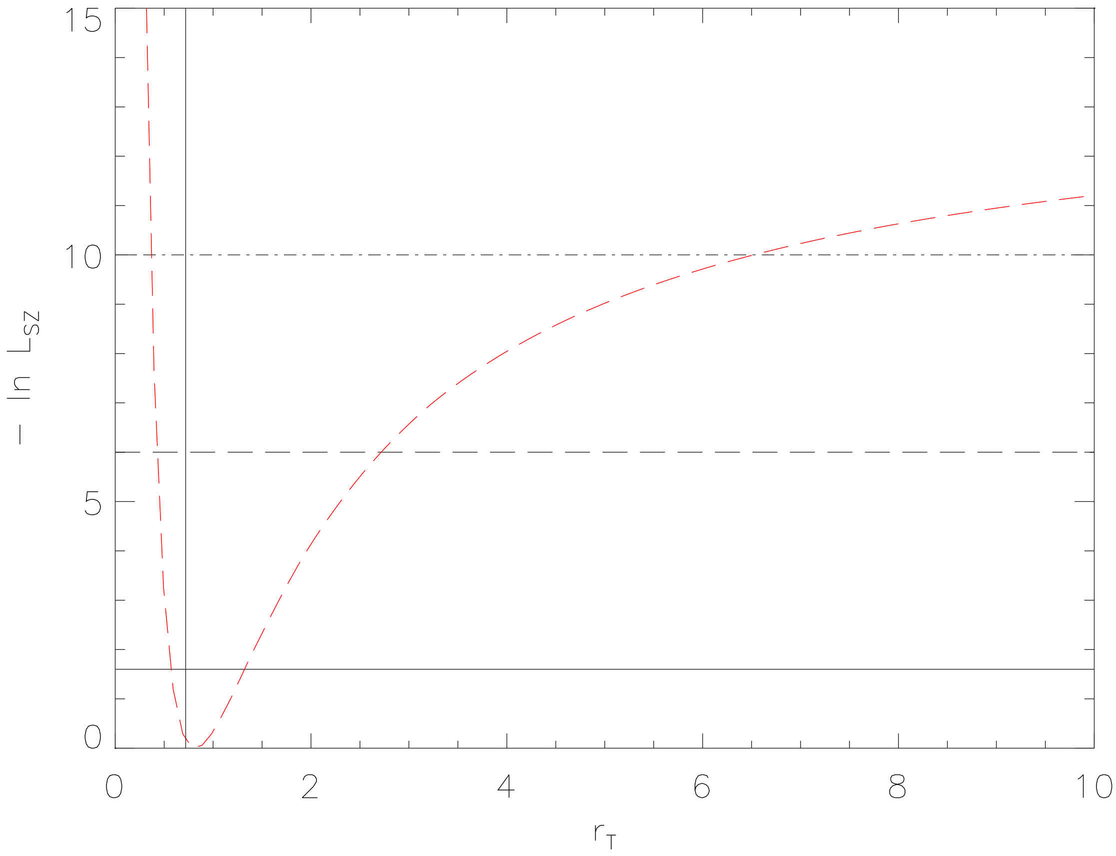

Fig. 9.— Same as Figure 8 but for the likelihood contours for fitting to the YZ projection of relaxed cluster AMRCL2 (red dashed line). The vertical solid line shows the best-fit value of $r_{\rm T}$ obtained by fitting directly to the temperature profile of AMRC2.

Table 1. Relaxed Clusters from AMR simulations

ID[a]	$M_{\rm vir}$[b]	$R_{\rm vir}$[c]	$r_{\rm core}$[d]	β[e]	$r_{\rm T}$[f]	δ[g]
AMRCL1	9.1E+14	2.0	0.107	1.05	0.91	1.6
AMRCL2	1.1E+15	2.1	0.144	1.00	0.73	1.6

[a] Galaxy Cluster ID.

[b] Virial mass in Solar Mass.

[c] Virial radius in Mpc.

[d] Core radius of the density model in units of $R_{\rm vir}$.

[e] β parameter describing the fall off of the density model.

[f] Scale parameter, $r_{\rm T}$, of the temperature model in units of $R_{\rm vir}$.

[g] δ parameter describing the fall off of the temperature model